Post Neutron Irradiation Annealing and Defect Evolution in Single Crystal Tungsten

D. Papadakis[1,2], K. Mergia[1,*], E. Manios[1], V. Chatzikos[1], S. Dellis[1] and S. Messoloras[1]

[1] *Institute of Nuclear and Radiological Sciences and Technology, Energy and Safety, NCSR Demokritos, Athens, 15310, Greece*

[2] *Department of Physics, School of Sciences, University of Athens, Athens, 15772, Greece*

Abstract

Single crystal W is offered for Physics understanding of irradiation induced defects and their annealing as its structure is well defined and it is almost defect free. W(100) single crystal was neutron irradiated to a damage of 0.11 displacements per atom at 600 °C and subsequently isochronally annealed from 700 up to 1500 °C in 100 °C steps. Irradiation causes the formation of dislocation loops and vacancy clusters and a 45% increase in hardness. After the annealing of 1500 °C the positron lifetime annihilation spectrum shows a defect free material and its hardness has been reverted to the pre-irradiation value and only clusters of Re, WRe and WO_2 have been detected by grazing incidence X-ray diffraction. The total line density of dislocations, number density of voids and their size versus annealing temperature have been determined. From hardness, the critical resolved stresses arising from dislocations and voids have been derived and correlated with their densities. The kinetics of defect annihilation versus annealing temperature is discussed.

Keywords: Radiation damage; tungsten single crystal; post-irradiation annealing; positron annihilation lifetime spectroscopy; electrical resistivity; hardness;

*Corresponding author: Dr Konstantina Mergia, email: kmergia@ipta.demokritos.gr

1 Introduction

Tungsten (W) is the main candidate material for plasma-facing components for current and future fusion devices due to its high melting temperature, high thermal conductivity, low tritium retention, good sputtering resistance, low swelling, thermal stress and shock resistance, and high-temperature strength [1–4]. Fission neutrons are usually used to simulate the neutron irradiation conditions in a fusion reactor [5–7]. The radiation induced damage mainly results in the formation of vacancy clusters, dislocations loops [8–10] and transmutation products [11–13]. The type and population of the induced defects are determined by the neutron irradiation conditions [7,14,15].

Aim of this work is the study of the recovery in single crystal (SC) tungsten after neutron irradiation damage at 600 °C. This, apart from being a challenging scientific problem, is of technological importance, as it could lead to a damage recovery procedure, extending thus the lifetime of tungsten plasma facing components through intermediate in-situ annealing cycles [16,17]. Single crystal recovery serves as a model system since no grain boundary or recrystallization phenomena will affect recovery after neutron irradiation. The first studies regarding recovery stages in W involve the recovery of neutron irradiated W materials using mostly resistivity measurements [18–26] and some field-ion microscopy studies [27,28]. More recent studies involving self-ion [29,30], proton [31,32], He [33–35] and neutron [36] irradiation at temperatures below 100 °C report vacancy migration in the range of 400 to 600 °C, with vacancy cluster coarsening when annealing at higher temperatures. Above 650 °C and up to 900 °C further coalescence of small vacancy clusters [29,31–33,36] along with dislocation loop growth and dislocation line rearrangement [30,33,35,36] occur, which could be termed as a stage IV recovery process. At higher temperatures, near 1000 °C dislocation loop annihilation is observed, most likely of interstitial type [32,36].

In this work W(100) SC, neutron irradiated to 0.11 displacement per atom (dpa) at 600 °C, has been isochronally annealed from 700 up to 1500 °C in 100 °C steps. The evolution of the microstructure is investigated through X-ray diffraction (XRD), electrical resistivity and positron annihilation lifetime spectroscopy (PALS) while the hardness and the depth-load curves were measured by depth sensing indentation using a Vickers and a spherical indenter, respectively. The evolution of the microstructure with increasing annealing temperature and the correlation between microstructure and micromechanics is discussed.

2 Materials and Methods

2.1 Materials – Neutron irradiation – Post Irradiation annealing.

The W(100) single crystal with purity of 99.999% was procured from MaTecK Material-Technologie & Kristalle GmbH in rod form. From the crystal rod, circular samples with diameter 12 mm and thickness around 1 mm were cut using electrical discharge machining (EDM). After cutting, the samples were mechanically polished from both sides using diamond suspension for removing the surface damage induced by the EDM cutting. At the final stage, colloidal silica was used in order to obtain mirror quality surface. The resulting thickness of the samples was in the range from 0.5 to 0.6 mm (almost half of the sample was

removed). These samples, together with other W grades, were irradiated in the BR2 reactor, at SCK CEN, Mol, Belgium. The sample used for the post irradiation annealing was irradiated at 600 °C to a neutron fluence of about 5.4×10^{20} n/cm^2 for E>0.1 MeV corresponding to a dose of 0.11 displacements per atom (dpa) using a displacement energy, E_d, of 55 eV, following the recommendation of IAEA standard [37]. More details about the neutron irradiation can be found in [38]. The annealings were performed under high vacuum (~10^{-6} mbar) in the range from 700 to 1500 °C and in steps of 100 °C. The irradiated samples along with non-irradiated ones were annealed at each temperature for 24 hours. Subsequently they were cooled down and characterized with different techniques (see section 2.2) before the next temperature anneal.

Hereinafter, we use the following terms a) *non-irradiated sample* refers to the initial state without irradiation and any heat treatment, b) *as irradiated sample* after the 0.11 dpa at 600 °C irradiation and before any annealing, c) *annealed irradiated sample* refers to the irradiated sample after annealing at a specific temperature (to be noted that the annealing at different temperatures is performed on the same sample) and d) *control sample* designates the non-irradiated sample annealed at different temperature with the same conditions as the annealed irradiated sample. It is noted that the control samples had the same surface treatment as the irradiated samples. Further an electropolished sample was used in order to assess any surface effects. Annealing of the control sample at 600 °C has no effect on the measured properties.

2.2. **Characterization techniques**

The W(100) sample in its non-irradiated state, in the as-irradiated and after each annealing step was characterized with the techniques outlined below. X-ray diffraction techniques are aimed at the observation of structure evolution after each annealing step and the determination of any possible agglomeration of transmutation products in the form of crystalline phase. Positron annihilation lifetime spectroscopy was employed for the determination of the open volume defects (dislocations, vacancies, voids) and the assessment of the defect interactions as a function of the annealing temperature. Resistivity measurements reflect the temperature evolution of both open and close volume defects and transmutation products. Finally hardness measurements aimed at correlating the mechanical properties of the material with the evolving defect structure.

2.2.1. X-Ray Diffraction (XRD) and Grazing Incidence X-ray diffraction (GIXRD)

The crystalline structure was evaluated by X-ray diffraction (XRD) measurements carried out at room temperature using Bruker D8 diffractometer with a Cu K_α X-ray source, a parallel beam stemming from a Göbbel mirror and a scintillator detector. In addition, Grazing Incidence XRD (GIXRD) measurements were carried out at a grazing angle of 1.0 degree in order to increase the sensitivity for the detection of other phases.

2.2.2. Positron Annihilation Lifetime Spectroscopy (PALS)

Positron Annihilation Lifetime Spectroscopy measurements were carried out at room temperature, using the Ortec® PLS-system. More details on the experimental setup can be found in [39]. The data analysis was performed using LT10 software [40,41]. From the analysis of the data, the lifetime, τ_i, of each type i of defect and the probability, I_i, of the positron to be annihilated in type i defect ($\sum I_i = 1$) are determined.

2.2.3. DC Resistivity

Electrical resistivity was measured employing the collinear 4-point probe (4PP) method using Keithley 2182A nanovoltmeter and Keithley 6221 AC and DC source. In order to eliminate the thermoelectric voltage contribution in the measurements, the current source and the nanovoltometer are operated in tandem utilizing "Delta Mode". The measured resistance is converted to resistivity through a geometric factor, dependent on the sample's size [39].

2.2.4. Hardness

Depth-sensing indentation experiments were performed employing a NANOVEA's mechanical tester using a Vickers indenter. The maximum load was set at 3 N, and the (un)loading rate was 20 N/min. A dwell time of 200 s was applied before starting the unloading process. The loading rate was selected after a series of preliminary indentation tests to achieve stability in the hardness values. The holding time was chosen such as to attain equilibrium conditions, i.e. almost no change of the indentation depth. A set of six indentation tests, spaced by 200 μm, were performed for each measurement. An optical microscope was used to select the indented area free from visible defects. The Vickers hardness, H_V, of the samples was calculated using the contact area, A_C, of the indenter, determined from optical microscopy images of the residual imprint after the indentation tests and the maximum applied force, $F_{\max}$, employing the equation

$$H_V = \frac{F_{\max}}{A_C} = \frac{2F_{\max}}{d_{mean}^2}\sin\left(\alpha/2\right) \quad (1)$$

where d_{mean} is the mean diagonal length measured from corner to corner on the residual impression in the specimen surface and $a = 136°$ is the face angle of the square-based diamond pyramid of the Vickers indenter.

3. Results and Discussion

The discussion of the experimental results after annealing is correlated with the observed microstructure and properties of the non-irradiated and the as irradiated sample (section 3.1). As mentioned above, a non-irradiated sample is also heat treated together with the irradiated

one and it is characterized also after each annealing step and in the following text it will be referred as the control sample.

In the experimental data graphs the datum point displayed for 600 °C corresponds to the as irradiated material (before any annealing) and it is indicated as such. As a tool to understand and discuss the experimental data, jointly with them an empirical equation is displayed of the form $y(T) = y_0\, exp\left\{-\left(\frac{T(°C)-T_0}{\Delta T(°C)}\right)^2\right\}$, where T the annealing temperature, i.e $T > T_{irr}$. The form of empirical equations is based on the observation that annealing of the defects for each one of their measured properties starts mainly after the first annealing temperature ($T_0 = 700$ °C) and that this form provides a good correspondence with all the measured values versus annealing temperature. The only Physics implication is that there is an energy activation of the process connected with T_0 and that the process has been mostly completed within the temperature range $T_0 + \Delta T$. To be more specific a defect annealing temperature, T_{anneal}, is defined such as $\frac{y(T_{anneal})}{y_0} \sim$ (i.e. less than 5% of the defects remain). The experimental $y(T)$ values and correspondingly the values of T_0 and ΔT are function of type and number of defects and their effect on the measured property. Thus, these values obtained from different techniques are expected to be only in broad agreement as a consequence of the empirical description. The value of y_0 is compared and should be in good agreement with that of as the irradiated sample. It should be noted that the parameters of the empirical equations have not been obtained by least squares fit but by simulation (i.e. changing the parameters T_0, ΔT and y_0) in order to obtain the best overall description of the experimental data.

In section 3.1 the microstructure of the unirradiated and as-irradiated samples determined by TEM and published previously is summarized as the base for the discussion of the experimental results of the as-irradiated sample temperature annealing. The TEM results show that irradiation at 600 °C to a dose of 0.11 dpa results to the formation of dislocation loops and voids. In section 3.2 the crystal structure and the lattice stains are investigated by XRD and by GIXRD; it is observed after annealing at 1500 °C the agglomeration of Re, WOs_2 and WRe-σ phases. In section 3.2 the radiation induced resistivity is utilized in the determination of the dislocation number density versus annealing temperature. In section 3.3 from the radiation induced hardness the radiation induced critical resolved shear stress is obtained. Using the dispersed hardening barrier model and the total dislocation density determined by the resistivity, the individual components of critical resolved shear stress arising from dislocations and voids are determined versus annealing temperature. Finally in section 3.4 the PALS data are used to determine the behaviour of small vacancy clusters and in combination with the previous sections to evaluate the number density and size of the voids.

3.1. Microstructure of the unirradiated and as-irradiated sample

The unirradiated tungsten single crystal (W(100) SC) is defect free within the resolution of transmission electron microscopy (TEM) [7]. The microstructure of the W(100) SC irradiated to a similar dose of 0.18 dpa (E_d=55 eV) at 600 °C determined by TEM [7] is dominated by massive rafts of about 500 nm length, spaced between 200-500 nm and formed by the dislocation loops located within the rafts. The dislocation loops have a number density of $(5.4\pm1.1)\times10^{22}$ m^{-3} and an average diameter of (3.0±1.6) nm corresponding to a line density of $(5.0\pm2.9)\times10^{14}$ m^{-2}). Also dislocation lines with thirty times lower density $(1.6\pm0.4)\times10^{13}$ m^{-2}) are found. Voids with a density of $(8.1\pm3.2)\times10^{22}$ m^{-3} and an average diameter of (1.3±0.2) nm are randomly distributed within the matrix [7]. The TEM results of the as irradiated material will be utilized in the discussion of the experimental findings for comparison. This comparison should be viewed through the prism that simulations of collision cascades indicate that the sizes of radiation induced defects follow a power law and, thus, the majority of defects are below the threshold of TEM resolution [42]. The transmutation products have been evaluated by the FISPACT-II nuclide inventory code and TENDL-2019 nuclear database and are found to be 0.38 at% Re, 6×10^{-3} at% Os and 1.5×10^{-3} at% Ta. Therefore the main transmutation product is Re.

3.2. Microstructure evolution versus annealing (XRD, GIXRD)

XRD and GIXRD measurements were performed after each step of post irradiation (PI) annealing. In XRD measurements, due to the crystal orientation, only the (200) Bragg peak was observed in a θ-2θ scan. The GIXRD measurements were employed in order to increase the sensitivity to a possible sample poly-crystallinity and phase formation.

Assuming that the (200) Bragg peak and the resolution function are Gaussian, from the Full Width at Half Maximum (FWHM) of the (200) Bragg peak the standard deviation, σ_B, after each step of isochronal annealing of the irradiated sample has been calculated (Figure 1a) together with that of the control sample. Irradiation at 600 °C has resulted in the reduction of σ_B peak compared to that of the unirradiated sample.

The Bragg peaks of both irradiated and control samples annealed at 700 °C have the same width and this indicates that the Bragg peak width reduction from the non-irradiated state after irradiation at 600 °C is mainly a temperature effect. As the annealing temperature increases the standard deviation of the Bragg peak of the control sample decreases indicating that the coherence length increases i.e. stress fields are eliminated and at 1500 °C the Bragg peak width has reached the instrumental resolution. The same also occurs for the irradiated sample. However, the stress fields do not disappear completely and they remain even after annealing at 1500 °C (Figure 1b). This may be interpreted that a type of radiation induced defect has not been annealed and causes this remaining stress. The solid line in Figure 1b is described by the equation $\Delta\sigma_B(\text{mins}) = 0.6\cdot\left[1-exp\left(-\frac{T(°\text{C})-700}{150}\right)\right]$. The asymptotic value of the coherence length of the irradiated sample is about 500 nm which would correspond to a

defect density of the order of ~10^{19} m^{-3}. The stress fields of the irradiated material have reached a steady state after the annealing at 1100 °C.

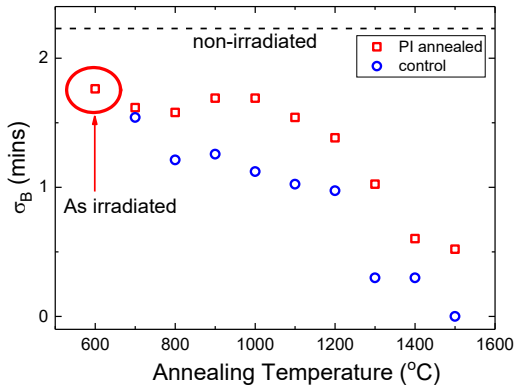

Figure 1a. Standard deviation, σ_B, of the (200) Bragg peak after each annealing step, irradiated (□), control sample (○), non-irradiated (dashed line).

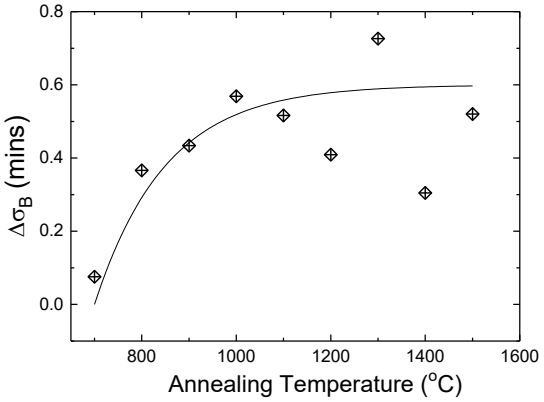

Figure 1b. Difference between the standard deviation of (200) Bragg peak of irradiated and control sample $\Delta\sigma_B = \sigma_B(\text{irradiated}) - \sigma_B(\text{control})$. Line: see text for details.

In the GIXRD spectrum only after PI annealing at 1500 °C, additional Bragg peaks to those of W were observed (Figure 2). These have been assigned to polycrystalline bcc Re as well as WOs_2 and WRe-σ phases with the two latter being both tetragonal within $P4_2/mnm$ space group (Figure 2). These additional Bragg reflections have not been observed in the annealing treatments below 1500 °C, indicating that a mechanism involving the local increase of Re and Os concentration is at play. It is noted that in a perfect W(100) SC no Bragg peaks should have been observed in GIXRD mode. Their presence, also in the non-irradiated and control samples, shows that in the SC material small polycrystalline regions exist which are not revealed in the XRD mode of measurement. The crystallite size of all the polycrystalline phases detected, as determined from the width of the Bragg peaks corrected for the instrumental resolution and using the Scherrer equation, varies in the range of 30 to 50 nm.

The calculated Re concentration is around 0.38 at% and thus the sigma phase WRe is not expected according to the phase diagram [43]. Precipitation is, however, observed in neutron irradiated W at higher doses (usually > 1 dpa) and Re concentrations [14,44–46]. Possibly migrating vacancies pair with Re and Os. The attractive behavior between Re-vacancy and Os-vacancy has been shown by calculations [47]. These pairs as the temperature increases migrate and finally create second phases at the void surfaces (decoration). Probably some second phases have been formed below 1500 °C, but, because of their very low volume fraction, have not been observed.

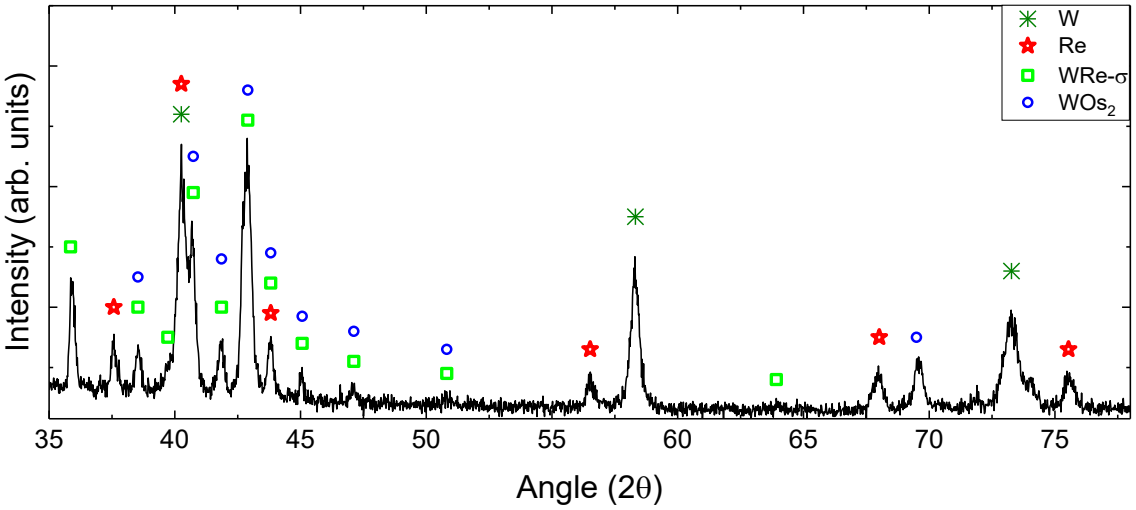

Figure 2. GIXRD after annealing at 1500 °C. The phases of W, Re, WRe-σ and WOs_2 are detected.

3.3. DC Resistivity

After irradiation the resistivity increases from $R_{non-irr} = (5.46 \pm 0.03)\ \mu\Omega\cdot\text{cm}$ to the value $R_{irr} = (6.41 \pm 0.05)\ \mu\Omega\cdot\text{cm}$. The resistivity of the control sample does not show any annealing temperature dependence and has a mean value over all the annealing temperatures of $\langle R_{control}(T)\rangle = (5.48 \pm 0.02)\ \mu\Omega\cdot\text{cm}$. In Figure 3 the radiation induced resistivity (RIR) $RIR(T) = R_{irr}(T) - \langle R_{control}(T)\rangle$ is shown. From Figure 3 it is observed that there is a slight decrease in the RIR up to the annealing temperature of 800 °C, then follows a much faster decrease and finally after 1100 °C the RIR remains constant. The temperature dependence of RIR can be described by the empirical equation $RIR(T) = RIR_{\infty} + R_0\, exp\left[-\left(\frac{T(°C) - 700}{\Delta T}\right)^2\right]$ with $RIR_{\infty} = 0.46\ \mu\Omega\cdot\text{cm}$, $R_0 = 0.44\ \mu\Omega\cdot\text{cm}$ and $\Delta T = 260$ °C.

Irradiation has produced voids, dislocations and transmutation products. Using the Matthiessen's rule [48], RIR, can be expressed as

$$RIR = RIR_{void} + RIR_{disl} + RIR_{trans} \quad (2)$$

where RIR_{void}, RIR_{disl} and RIR_{trans} are the contributions of voids, dislocations (both loops and lines) and transmutation products, respectively. Initially will be discussed the RIR of the as irradiated sample from which the strength of the different contributions can be determined since the sizes and the densities of the different defects have been measured by TEM (see 3.1).

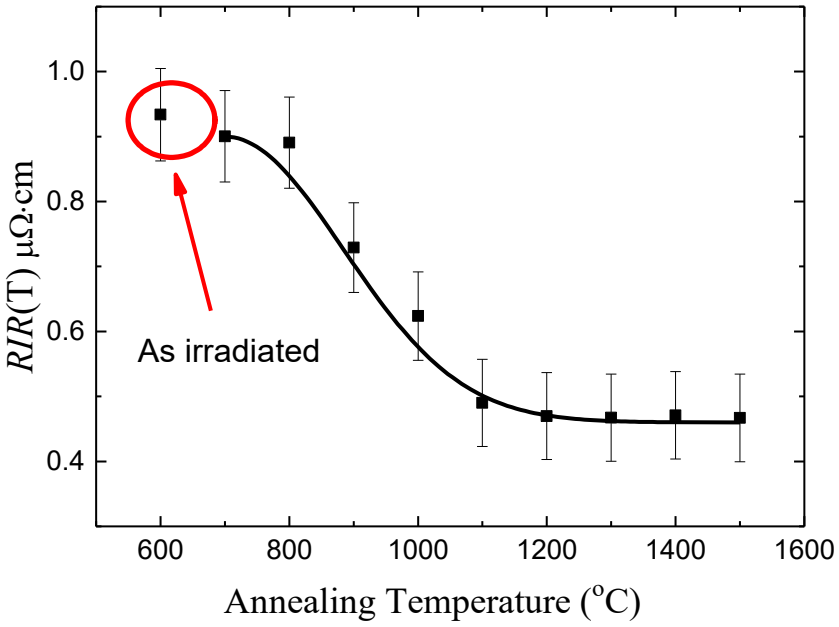

Figure 3. Radiation induced resistivity versus annealing temperature.
Line: see text for details.

The contribution of voids to RIR in the as irradiated sample can be calculated [49–51] using their diameter and number density determined by TEM and the specific resistivity [52] and it is found to be 10^{-2} μΩ·cm. Therefore, the contribution of voids to the measured RIR of the as irradiated sample is less than 1% and their contribution can be ignored.

The contribution of the transmutations products to the measured RIR can be calculated from their concentrations (see 3.1) and the specific resistivity of rhenium P_{Re} (~1.3 μΩ·cm/Re at.%) [53] and osmium P_{Os} (~5 μΩ·cm/Os at.%) [54] (Ta may be ignored as its concentration is much lower), and it is found to be $RIR_{trans} = 0.52$ μΩ·cm. This is close to the asymptotic value ($RIR_{\infty} = 0.46\ \mu\Omega\cdot\mathrm{cm}$) obtained from the experimental data. If we take into account the errors in calculating the resistivity arising from the transmutation products and that part of them that have been agglomerated as shown by GIXRD (section 3.2), thus resulting in lower resistivity, we may conclude that the value of RIR_{∞} arises from the transmutations products. Therefore, it can be deduced that $RIR(T) - RIR_{\infty}$ arises solely from dislocations lines and loops, i.e.

$$RIR(T) - RIR_{\infty} = RIR_{disl} = P_{DSR} \cdot N_{disl} \qquad (3)$$

where N_{disl} is the total density of dislocation lines (both loops and lines) and P_{DSR} the specific resistivity of dislocations (3×10^{-23} Ω·m^3) [39]. Using Eq. (3) and the measured values of RIR_{disl} the total dislocation line density values have been calculated and they are presented in Figure 4. The total dislocation line density (from both loops and lines) of the as irradiated

material determined by the resistivity measurements is (1.6±0.2)×10^{14} m^{-2} and it is in good agreement with that determined by TEM ((5.2±2.9)×10^{14} m^{-2}, see section 3.3) taking into account the errors. The line in Figure 4 corresponds to the equation $N_{disl}(T) = 1.5\times10^{14}\cdot exp\left\{-\left(\frac{T(°C)-700}{\Delta T_{disl}}\right)^2\right\}$ m^{-2} where T is the annealing temperature in °C and $\Delta T_{disl} = 260\,°C$. The temperature at which about less than 5% of the initially neutron irradiation produced dislocations is T_{anneal} ~ .

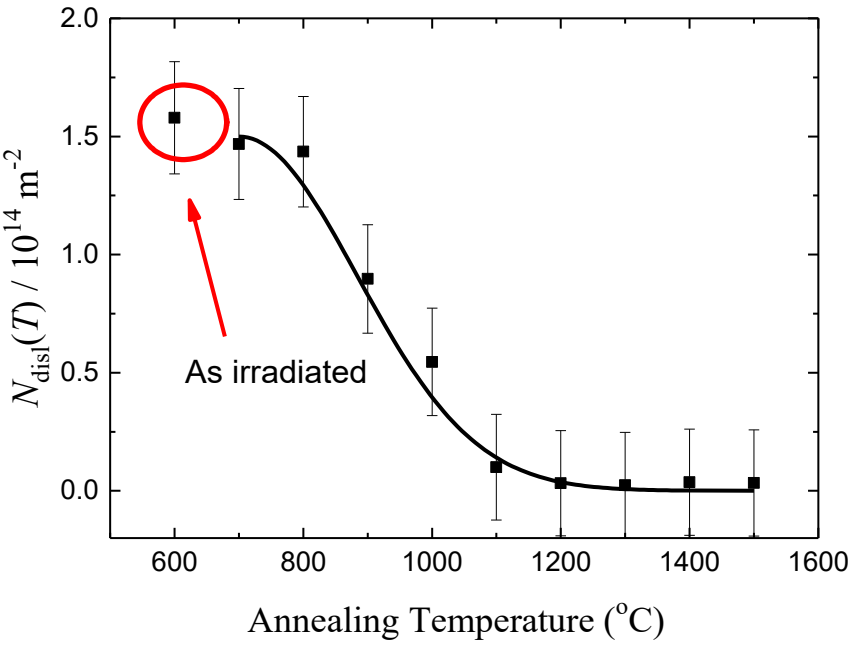

Figure 4. Total dislocation line density (loops and lines) determined by resistivity. Line: see text for details.

3.4. Vickers hardness

The Vickers hardness of a single-crystal sample depends on the angle between the diagonals of the indenter and the in-plane crystallographic axes [55]. The highest hardness value is found when the indenter's diagonal is parallel to <010> direction, whereas the lowest hardness value when the indenter's diagonal is parallel to <011> direction (see [56] for more details). This dependence can be explained through the availability of slip planes on BCC crystals [57,58]. The modulation itself is caused by the available slip systems and the geometry of the indenter [59]. In this work, the mean hardness over all the different directions of the indenter diagonal will be utilized.

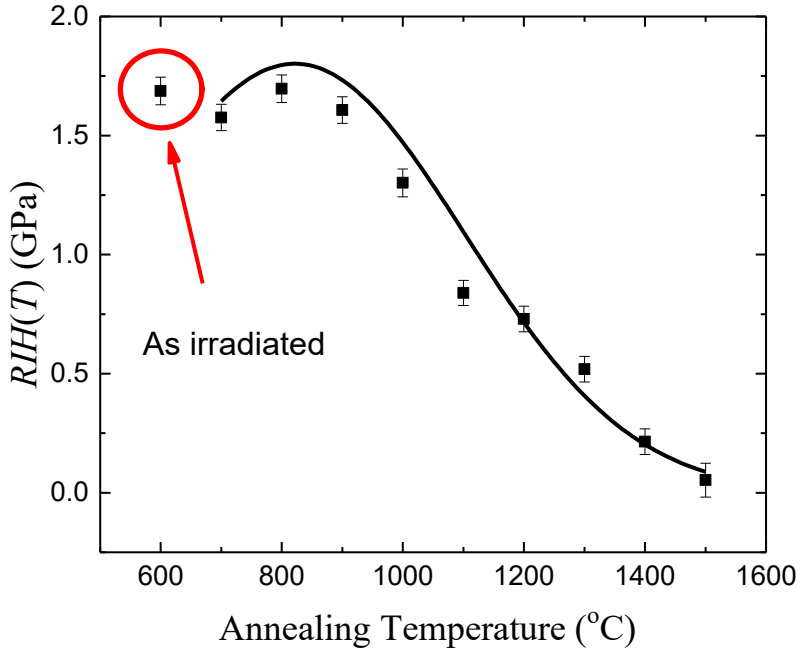

Figure 5. Radiation induced hardness versus annealing. Line: Calculated from $\Delta\tau_{CRSS}^{calc}$ (Fig. 7) and eq. (4).

The hardness of the control sample does not change with annealing temperature giving a mean value over all the annealing temperatures of (3.29±0.04) GPa which is close to that of the non-irradiated sample ($H_{non-irr} = (3.34 \pm 0.05)$ GPa). The radiation induced hardness $RIH(T) = H_{irr}(T) - H_{non-irr}$ after each annealing step is presented in Figure 5. The radiation induced hardness can be associated with the radiation induced critical resolved shear stress (CRSS), $\Delta\tau_{CRSS}$, as

$$RIH = k\,\Delta\sigma = k\,M\Delta\tau_{CRSS} \tag{4}$$

where $\Delta\sigma$ the yield strength [60], k is a factor of 3.2 for tungsten [61] and for M the value of 3.06 for non-textured BCC and FCC crystals [62] will be used. Using eq. (4) and the measured values of RIH the radiation induced critical resolved shear stress has been determined (Figure 6). As RIH at 1500 °C is almost zero, it is inferred that the contribution of the transmutations products is negligible to RIH as these are the only remaining defects at this temperature. Therefore the CRSS can be attributed solely to dislocations and voids. In figure 6 the contributions arising from dislocation and voids CRSS (τ_{disl}^{calc} and τ_{voids}^{calc}), as will be demonstrated below, are displayed.

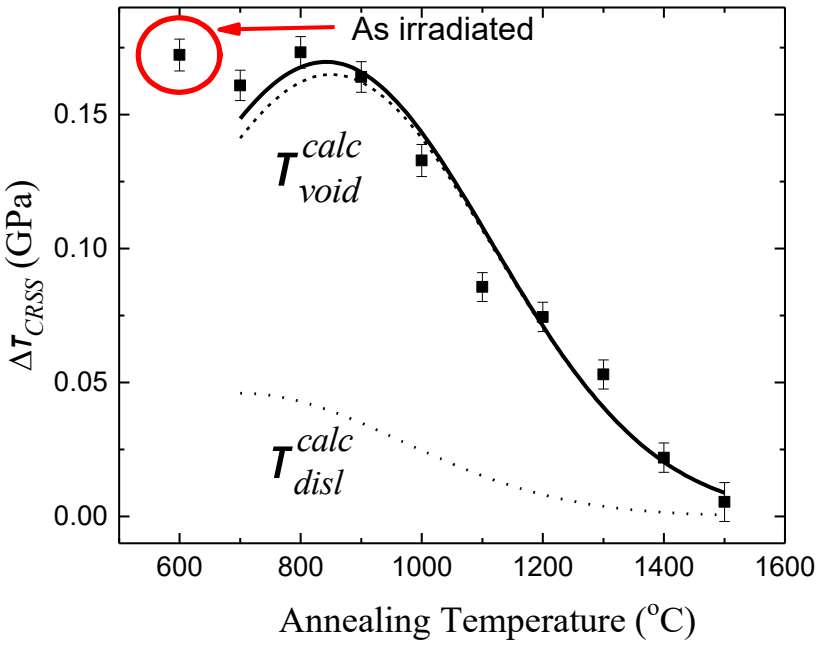

Figure 6. Radiation induced critical resolved shear stress calculated from radiation induced hardness, RIH, and eq. (4). Dotted line: Contribution of dislocations, τ_{disl}^{calc} (line of Figure 7). Dashed line: Contribution of voids, τ_{voids}^{calc} (line of Figure 8). Continuous line: Sum of the contribution from dislocations and voids $\Delta\tau_{CRSS}^{calc} = \sqrt{\left(\tau_{disl}^{calc}\right)^2 + \left(\tau_{voids}^{calc}\right)^2}$.

Assuming that the lattice friction stress does not change with irradiation, the induced CRSS arises from the radiation defects, i.e. dislocation loops and lines and voids, and it can be written according to the dispersed hardening barrier (DHB) model as [61,63]

$$\Delta\tau_{CRSS}^2 = \tau_{line}^2 + \tau_{loop}^2 + \tau_{void}^2 = G^2 b^2 \left(h_{line}^2 \rho_{line} + h_{loop}^2 \rho_{loop} + h_{void}^2 \rho_{void}\right) \quad (5)$$

where G is the shear modulus (159 GPa), b is the Burgers vector (0.274 nm), h_{line} is the dislocation line strength coefficient equal to 0.26 [64], h_{loop} has the value of 0.15 [36], h_{void} is the defect strength of voids which is dependent on their size [39] and ρ is the obstacle length density ($\rho = N \cdot d$, N the defect number density and d the defect size). As the strength of dislocation lines and loops are very close and also the density of loops in the as irradiated sample is 30 times larger than that of the lines eq. (5) can be approximated as

$$\Delta\tau_{CRSS}^2 = G^2 b^2 \left(h_{line}^2 \rho_{line} + h_{loop}^2 \rho_{loop} + h_{void}^2 \rho_{void}\right) \approx G^2 b^2 h_{loop}^2 \rho_{disl} + \tau_{void}^2 \quad (6)$$

where $\rho_{disl} = \rho_{loop} + \rho_{line}$. From the total dislocation line density determined by the resistivity (Fig. 4) the CRSS arising from all the dislocations (loops and lines), τ_{disl}, can be determined

(see Figure 7). The continuous line corresponds to the equation $\tau_{disl}^{calc}(\text{GPa}) = 0.046 \cdot exp\left\{-\left(\frac{T(°\text{C}) - 700}{380}\right)^2\right\}$ where T is the annealing temperature in °C and 700 °C the first annealing temperature. τ_{disl}^{calc} is displayed as the dotted line in Figure 6 indicating the contribution of the dislocations to the total CRSS. Comparing with RIR results (Figure 3) we observe that T_0 is the same, whereas ΔT from CRSS is higher than that of RIR. This reflects the difference in the sensitivity of the two methods in the density of dislocations.

From eq.(6) the CRSS arising from voids is calculated i.e. $\tau_{void} = \sqrt{\Delta\tau_{CRSS}^2 - \tau_{disl}^2}$ and it is presented in Figure 8. The continuous line corresponds to the equation $\tau_{void}^{calc}(\text{GPa}) = 0.165 \cdot exp\left\{-\left(\frac{T(°\text{C}) - 850}{380}\right)^2\right\}$ which is also displayed as the dashed line in Figure 6 indicating the contribution of the voids to the total CRSS.

The continuous line in Figure 7 has been calculated by adding the contributions of both dislocations and voids to the irradiation induced CRSS i.e. $\Delta\tau_{CRSS}^{calc} = \sqrt{\left(\tau_{disl}^{calc}\right)^2 + \left(\tau_{void}^{calc}\right)^2}$. From $\Delta\tau_{CRSS}^{calc}$ and eq. (4) the calculated radiation induced hardness, RIH^{calc}, is obtained which is presented as the continuous line in Figure 5, and from this the hardness can be calculated as $H_{irrad}^{calc}(T) = RIH^{calc} + H_{unirr}$.

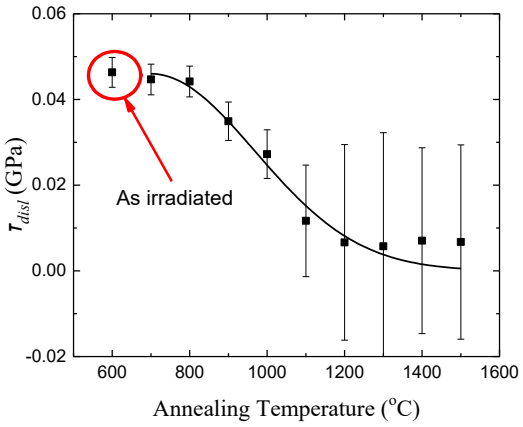

Figure 7. CRSS arising from dislocations calculated from $\tau_{disl} = Gbh_{loops}\sqrt{\rho_{disl}}$, where ρ_{disl} obtained from the resistivity measurements (Figure 5).

Continuous line: τ_{disl}^{calc} (see text for details).

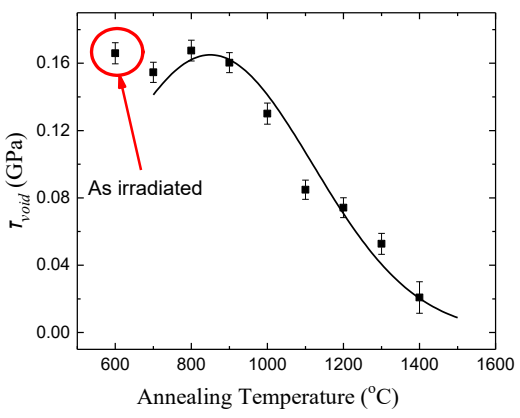

Figure 8. CRSS arising from voids, calculated from equation $\tau_{void} = \sqrt{\Delta\tau_{CRSS}^2 - \tau_{disl}^2}$ ($\Delta\tau_{CRSS}$ calculated from radiation induced hardness and eq. (5). Continuous line: τ_{void}^{calc} (see text for details).

3.5.Open volume defects from PALS

From the analysis of the experimental positron annihilation spectra a set of lifetimes $\tau_i^{exp}(T), i=1,...,n$ and corresponding intensities $I_i^{exp}(T)$ are determined. The intensities I_i^{exp} denote the probability of a positron to be annihilated in the interaction volume of the material by the defects designated by τ_i^{exp} and consequently $\sum I_i^{exp}=1$. The state of the material after an annealing at temperature T is described by a function $f_{def}(T), def=0,a,b,....$ denoting the fraction of defects $a,b,...$ within the material volume and f_0 corresponding to the defect free part of the material ($\sum f_{def}=1$). The corresponding lifetimes are denoted by τ_{def}. The probability of positrons to be annihilated within the interaction volume of the sample with the positron, I_{def}, from a specific defect fraction is $I_{def}=p_{def}f_{def}$ and $\sum p_{def}f_{def}=\sum I_{def}(T)=1$, where p_{def} the probability of positron annihilation with the specific defect. A measured lifetime, τ_i^{exp}, may correspond to a specific, τ_{def}, open volume defect e.g. dislocation, void or to a group of defects having close lifetimes and which cannot be distinguished in the spectrum due to resolution limitations. Thus, in correlation with known from the literature lifetimes for specific defects, the measured $\tau_i^{exp}(T)$ and consequently the corresponding intensities $I_i^{exp}(T)$ can be assigned to one or more defects. The evolution of the defect structure versus annealing is described, as discussed in section 3.3, by heuristically derived equations of the form $I_{def}(T)=c\,exp\left\{-\left(\frac{T-T_0}{\Delta T}\right)^2\right\}$ to be compared with the experimental ones and $I_0=1-\sum_{a,b,...} I_{def}$. In case a specific experimental lifetime τ_k^{exp} has been assigned to more than one defect i.e. for example a',b' then the function $\sum_{a',b'} I_{def}(T)$ is compared with the experimental I_k^{exp} and the mean lifetime

$$\langle\tau\rangle=\frac{\sum_{a',b'} I_{def}(T)}{\sum_{a',b'}\left(I_{def}(T)/\tau_{def}\right)} \tag{7}$$

with the experimental τ_k^{exp}.

Before discussing the experimental PALS results, a brief literature review of the positron lifetimes of the relevant irradiation defects in W is advantageous. The lifetime, τ_0, for the defect free material is reported in the range of 100-116 ps [65–72]. Dislocation lifetime varies from 130 to 180 ps [35,36,65–71]. Mono- or di- vacancies have a lifetime in the range of 160-200 ps and small vacancy clusters between 200 to 230 ps, [67]. The calculated positron lifetime for voids increases with their size and reaches a saturation value of around 500 ps for a void containing around 40 vacancies [67,73].

The PALS spectrum of the unirradiated W single crystal sample after electropolishing exhibits a lifetime $\tau_0 = 114$ ps, as reported in our previous work [38], which is in agreement with that reported for the defect free material. However, the determined lifetime for the unirradiated and mechanically only polished control sample is around $\tau_1 = 154$ ps.

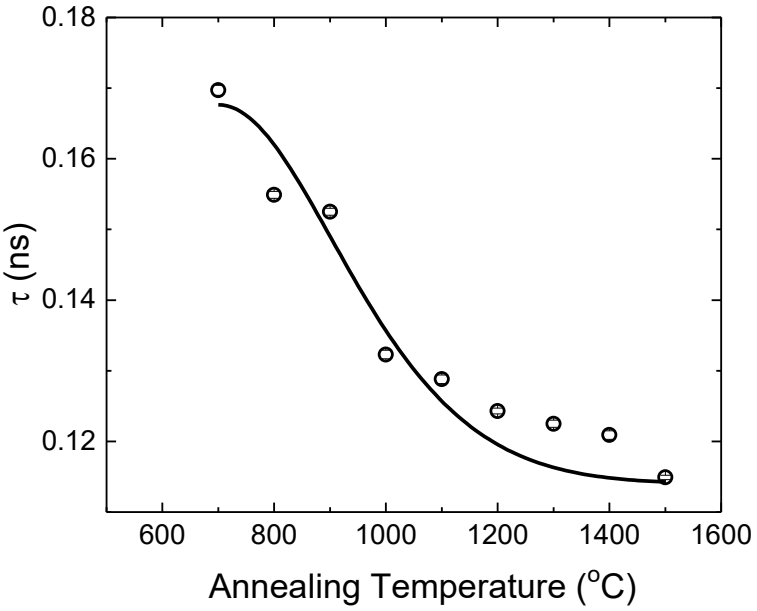

Figure 9. Lifetime of the control sample versus annealing temperature. Points (**O**): Experimental data. Continuous line: Simulation (see text for details).

Upon annealing the lifetime of the control sample increases from the value of 154 ps (not shown) to 170 ps after annealing at 700 °C and upon further annealing is reduced with increasing temperature reaching the value of 112 ps ~~after annealing~~ at 1500 °C (Figure 9). These observations lead to the conclusion that the observed lifetime, τ, is an average of the lifetimes of the defect free material and that of defects arising from the mechanical treatment and as these defects are annealed the lifetime decreases to the value of the defect free material. The continuous line in Figure 9 has been simulated using eq. (7) and assuming two lifetimes that of the defect free material ($\tau_0 = 114$ ps) and of a defect type with lifetime $\tau_a = 210$ ps having a temperature dependence found by simulations as $I_a(T) \sim \left(\frac{T-700}{360} \right)^2$. The lifetime τ_a employed in the simulation is close to that corresponding to dislocations and mono/di-vacancies and reflects dislocation and mono/di-vacancy formation by the mechanical polishing. The increase of the positron lifetime from 154 ps to 170 ps after annealing at 700 could be due to vacancy de-trapping from dislocations.

Two lifetimes were needed in order to describe the PALS spectra for the irradiated sample, a short one, $\tau_1^{\exp} = (177 \pm 4)$ ps, and a long one, $\tau_2^{\exp} = (478 \pm 9)$ ps. After the annealing at 1500

°C, only the short positron lifetime (Figure 10a) is observed and its value is close to that of the defect free material. From this, it may be concluded that the short positron lifetime is an average, as discussed in the first paragraph of this section, of the defect free material and defect(s) with positron lifetimes around 200 ps or a little higher. From the literature review of the positron lifetimes mentioned above, these two defects could be dislocations, mono or di-vacancies or very small vacancy clusters. The long positron lifetime, τ_2^{exp}, can be attributed to large vacancy clusters or voids having a size larger than 1 nm (Figure 10b).

From the annealing temperature dependence of I_1^{exp} (Figure 11a) and τ_1^{exp} (Figure 10a), there is the suggestion that there are three annealing mechanisms which imply the kinetics of three different defects. As τ_1^{exp} after 1500 °C attains the value of the defect free material we have to accept that I_1^{exp} includes positron annihilation in the defect free part of the material. Therefore, we make the correspondence of experimental data and simulations as $I_1^{exp} \rightleftarrows \quad + I_a(T) + I_b(T)$. According to the discussion in paragraph two of this section, the determined τ_1^{exp} has to be correlated with the mean time of the lifetimes of three sources of positron annihilation.

For the short lifetime, depicted in Figure 10a, we observe that there are two annealing mechanisms centered at around 700 and 1100 °C. Similar conclusions are drawn for the lifetime τ_2^{exp}. The long lifetime has been assigned, as discussed above, to voids. Therefore, these two mechanisms could be assumed to be related to voids and, thus, the use of the association $I_2^{exp} \rightleftarrows \quad$ is justified.

Simulation equations of $I_a(T), I_b(T)$ and $I_c(T)$ have to be in agreement with the experimental data of I_1^{exp}, I_2^{exp} of Figures 11a and 11b and the experimental lifetime τ_1^{exp} via the equation of mean lifetime of defects a and b. The simulations equations displayed in Figure 11a are $I_a(T) = 45 \cdot exp\left\{-\left(\frac{T-700}{360}\right)^2\right\}$, $I_b(T) = 22 \cdot exp\left\{-\left(\frac{T-1050}{180}\right)^2\right\}$ and $I_0(T) = 1 - \left\{I_a(T) + I_b(T) + I_c(T)\right\}$. The simulated lifetime in Figure 10a is calculated from the equation $\frac{I_0(T) + I_a(T) + I_b(T)}{I_0(T)/\tau_0 + I_a(T)/\tau_a + I_b(T)/\tau_b}$ with $\tau_0 = 114$ ps (that of the defect free material) and $\tau_a = 210$ ps, τ_b=260 ps. Finally, the simulation equation for I_2^{exp} data is $I_c(T) = 44 \cdot exp\left\{-\left(\frac{T-750}{230}\right)^2\right\} + 50 \cdot exp\left\{-\left(\frac{T-1200}{180}\right)^2\right\}$ (Figure 11b).

The lifetime of defects of type a ($\tau_a = 210$ ps) is close to that of the dislocations and mono/di-vacancies. Their annealing temperature (the temperature at which only 5% of the initial defects remain) $T_{anneal} \sim 1300$ °C is also close to that found for dislocations from resistivity measurements (Figure 4, section 3.3). Therefore, defects of type a are assigned to

mainly dislocations both for those on the surface prior to irradiation (Figure 9) and those generated by the irradiation. It should be noted that resistivity measurements correspond to the bulk dislocations i.e. those generated by the neutron irradiation. On the contrary, positron annihilation is partly sensitive to the surface state and surface dislocations contribute to the spectrum.

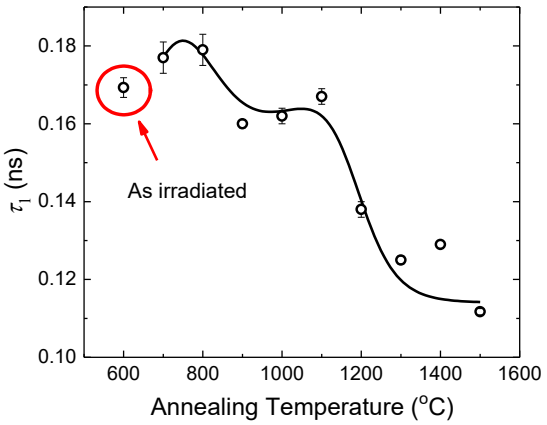

Figure 10a. Short lifetime, τ_1, versus annealing temperature. Points (**O**): Experimental data, Line: Simulation (for details see text).

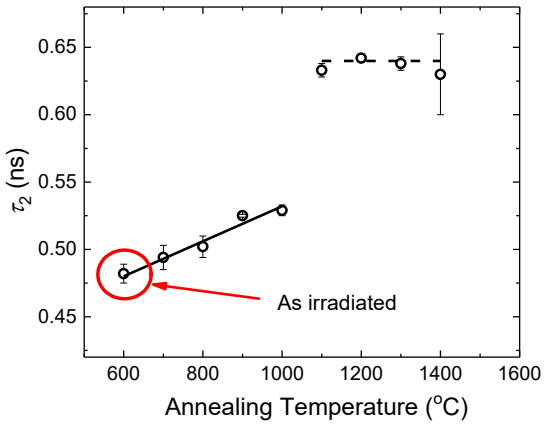

Figure 10b. Long lifetime, τ_2, versus annealing temperature. Points (**O**): Experimental data, Line: least squares, Dashed line: mean value.

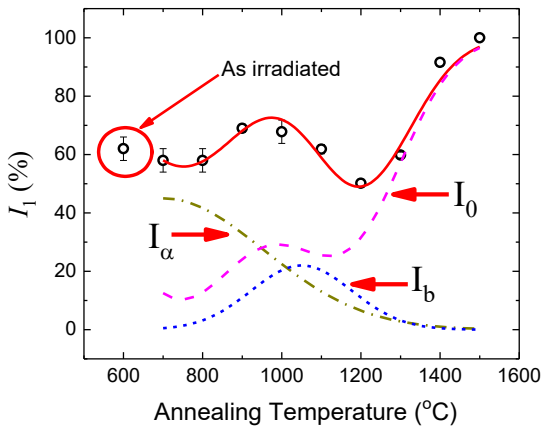

Figure 11a. Points (**O**): Experimental intensities, $I_1^{\exp}$, corresponding to the short lifetime, $\tau_1^{\exp}$. Dash-dot line: simulation of the contribution of the defects a, $I_a(T)$. Short-dash line: simulation of the contribution of the defects b, $I_b(T)$. Dash line: simulation of the contribution of the defect free material, $I_0(T)$. Continuous line: $I_0(T)+I_a(T)+I_b(T)$.

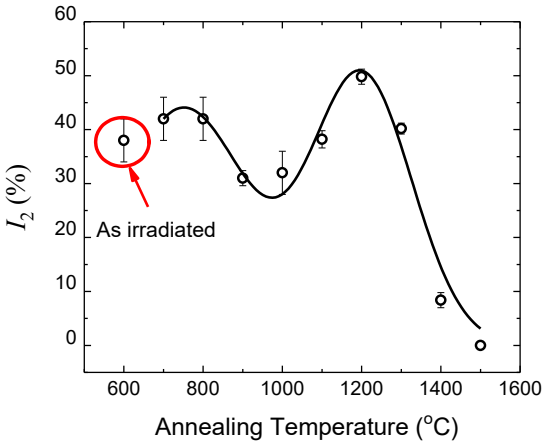

Figure 11b. Points (**O**): Experimental intensities, $I_2^{\exp}$, corresponding to the long lifetime, $\tau_2^{\exp}$.Continuous line: Simulation of $I_c(T)$.

The type b defect has not been caused by the neutron irradiation but it has been produced by the annealing. The lifetime of $\tau_b = 260\,\text{ps}$ corresponds to that of clusters of five to six vacancies [67]. Therefore, it is apparent the mono- and di-vacancies produced by irradiation at around 900 °C have increased mobility and coalesce into small vacancy clusters (Figure 10a). As the temperature is raised above 1100 °C their number decreases with $T_{anneal} \sim 1360\,°\text{C}$. This will be further addressed below in the discussion of the long τ_2^{exp} which has been associated to large vacancy clusters-voids.

The long lifetime, τ_2^{exp}, associated with voids, increases almost linearly (Figure 10b) from the value of about 480 ps of the as irradiated sample to 530 ps after annealing at 1000 °C. Annealing at 1100 °C causes an abrupt increase from 530 ps to around 630 ps, then up to 1400 °C the lifetime remains almost constant and after annealing at 1500 °C only the lifetime corresponding to the defect-free material is observed. Calculations of the lifetime of vacancy clusters show a linear behavior for lifetimes up to 425 ps corresponding to a cluster of around fifteen vacancies [67,73]. For larger vacancy clusters the lifetime remains constant and around 420 ps. Thus, the positron lifetime dependence on annealing temperature observed in Figure 10b is in accordance with the calculations. As the calculations show, an increase in the void size results in a positron lifetime increase as that observed up to 1000 °C. After a specific size of vacancy cluster the calculated lifetime has reached a plateau, i.e. remains constant independent of void size. The experimental data show that this size has been reached after the 1100 °C annealing. Positron lifetimes larger than 500 ps and above the theoretical saturation value of 420 ps, are reported in proton [32] and neutron [36] post-irradiation annealed tungsten and they were attributed to pick-off annihilation of ortho-positronium formed in large vacancy clusters, suggesting that the internal surfaces of the clusters may be partially decorated with impurities [36]. Figure 11b indicates that the fraction of voids remains almost constant up to 1300 °C, then sharply decreases to become zero at 1500 °C. Notwithstanding that the fraction of the voids remains almost constant the two peaks in Figure 11b in conjunction with Figure 10b indicate that there are two size distributions. At temperatures up to 900 °C the smaller sizes prevail, but after 1100 °C the larger ones do. From the simulated curve in Figure 11b we find that the annealing temperature for the smaller voids is around 1150 °C and for the larger clusters 1500 °C.

The determined lifetime τ_2^{exp} can be connected with the size of the voids by utilizing previous research on neutron irradiated tungsten in which both positron lifetime (not published) and TEM void size determination were made [7]. These data are depicted in Figure 12. From this correlation, we obtain a relationship connecting the average void size and PALS lifetime as

$$\left\langle d_{void}(\text{nm}) \right\rangle = 0.24 + 0.043\left(\tau_2^{exp}(\text{ps}) - 470\right) \tag{8}$$

The experimental validity range of eq. (8) connecting void size with positron lifetime τ_2 is for $450\,\text{ps} \le \tau_2 \le 620\,\text{ps}$ and the average systematic error in its application is around 15%. The diameter of voids corresponding to the linear part of the lifetime dependence on annealing temperature (Figure 10b) is given by $d = d_{\text{as-irradiated}} + C \cdot \left(T(°\text{C}) - 600\right)$ with

$d_{\text{as-irradiated}} \approx (1.0 \pm 0.4)$ nm and C=5×10^{-3} nm/°C (for example, the size of the voids at 1000 °C is 2.76 nm). We observe that the size of the voids for the as irradiated sample determined by TEM ((1.3±0.2) nm), section 3.1) and that obtained by the positron lifetimes ((1.0 ± 0.4) nm) are in good agreement within errors. The void size which corresponds to the constant positron lifetime (annealing temperatures 1100 °C and above) is around 7.4 nm. According to calculations [67], the lifetime for large voids is size independent, thus we may assume that the value of 7.4 nm reflects that of 1100 °C, the first temperature at which the large and constant lifetime is observed. For higher annealing temperatures very likely the size of the voids is larger. An increase in the size of voids coupled with a decrease in their number density after annealing at 1100 °C [74] or even 1300 °C and 1600 °C [75] is observed.

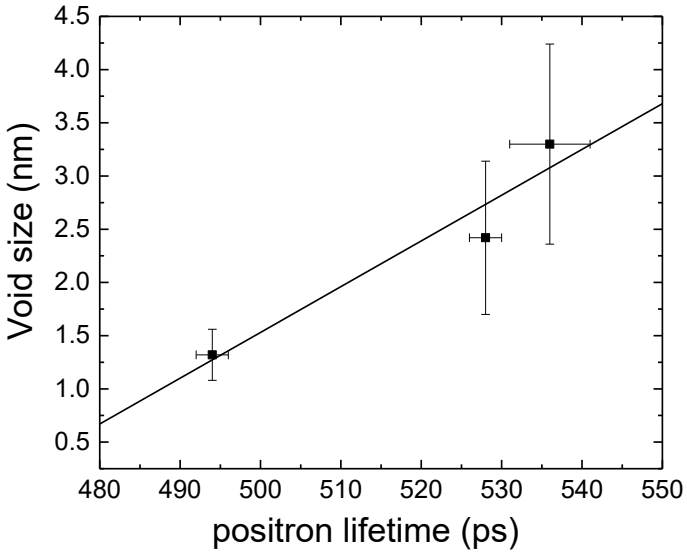

Figure 12. Void size determined by TEM [7] as a function of positron lifetime τ_2^{exp} determined from PALS measurements on W single crystal irradiated to 0.2 dpa (unpublished data).

From the discussion in the previous paragraph, we may conclude that we have extracted from the PALS data the size of the voids accurately and assuredly up to 1100 °C. The following analysis in which the determined size is utilized will be applicable to annealing temperatures up to 1100 °C.

Next, the CRSS derived from the hardness measurements and the assumption of the validity of the dispersion hardening barrier (DHB) model will be utilized in order to derive the number density and volume fraction of voids. Ought to be mentioned that the values that have been derived based on the DHB model correspond to the effect of voids on the measured hardness. Therefore, the results have to be in broad agreement with the findings of PALS but may differ in the details. The CRSS, τ_{void}, arising from voids (see Figure 8) will be utilized in order to determine the number density of voids as a function of the annealing temperature using the relationship

$$\tau_{void} = Gbh_{void}\sqrt{\rho_{void}} = Gbh_{void}\sqrt{N_{void}d_{void}} \quad (9)$$

The void obstacle strength, h_{void}, by utilizing experimental and calculated values [39] depends on the void size by the equation

$$h_{void} = Cd_{void}^{n} \quad (10)$$

where $C = (0.144 \pm 0.024)$ nm^{-n} and $n = 0.56 \pm 0.16$.

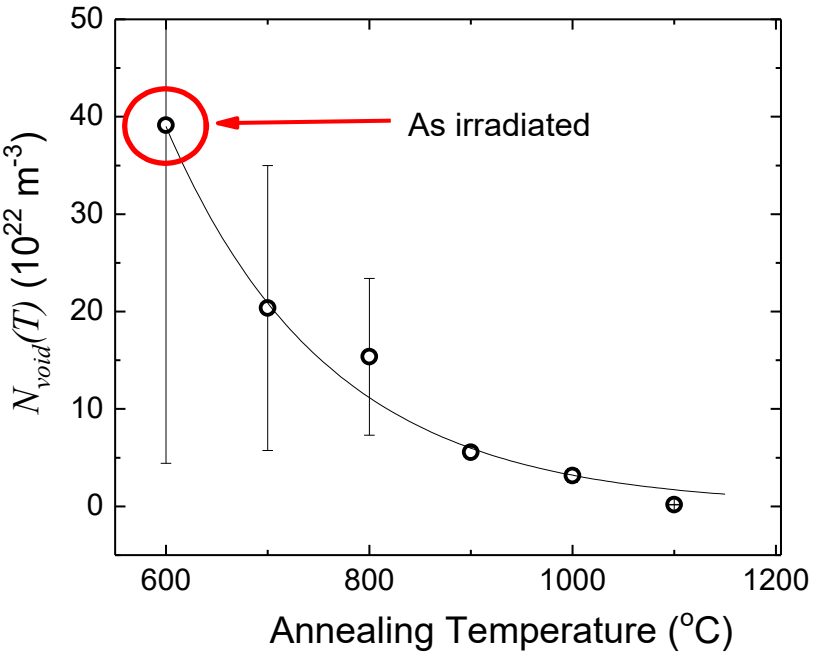

Figure 13. Number density of voids versus annealing temperature. Points (**O**): Experimental data, Line: Simulation (for details see text).

The number density of the voids, N_{void}, using the experimental values of τ_{void} and d_{void} (calculated from τ_2^{exp} and eq. 8) and eqs. 9 and 10, is presented in Figure 13. The N_{void} of the as irradiated sample obtained by this procedure is (39±34)×10^{22} m^{-3} which is in fair agreement with the value obtained by TEM ((8.1±3.2)×10^{22} m^{-3}) taking into account the large errors and the fact that voids of ~1 nm size are barely within TEM resolution [42]. It is noted that above 1100 °C no data are shown in Figure 13 because of the saturation of the positron lifetime (Figure 10b) that does not allow the determination of the void size. In any case, it may be assumed that the number density of voids continuously decreases up to 1500 °C the temperature at which a defect free material is observed by PALS. The continuous line in Figure 13 corresponds to the equation $N_{void}(T) = 39\times10^{22} \cdot exp\left(-\frac{T(^{\circ}\mathrm{C}) - 600}{160}\right)$ m^{-3}. The experimental data and the empirical equation show a fast exponential decrease of the number of voids generated by neutron irradiation. The temperature at which 5% of neutron generated voids remains is $T_{anneal} \sim 1080$ °C. From PALS data, as discussed above, we find that the

annealing temperature for the smaller voids (Figure 11b) is around 1150 °C. However, from PALS the annealing temperature for the larger clusters is around 1500 °C. This value is in excellent agreement with the annealing temperature from τ_{void}^{calc} (Figure 8) which is 1510 °C. Therefore the number density of voids calculated above is weighted towards smaller voids.

Finally, from the void size and their number density the volume fraction of voids

$$f_{void} = \frac{4\pi}{3}\left(\frac{d_{void}}{2}\right)^3 N_{void} \tag{11}$$

can be determined and is presented in Figure 14. The continuous line corresponds to the heuristic equation $f_{void}(T) = 0.048 \cdot exp\left[-\left(\frac{T(°C)-900}{250}\right)^2\right]\%$. The $T_{anneal} \sim 1330$ °C for the volume fraction is in better agreement with the values obtained from PALS and hardness measurements. From the TEM data, the calculated volume fraction of voids for the as irradiated sample is (0.011±0.008)%, which is within errors in agreement with the value derived from the combination of the PALS and hardness measurements (Figure 14), validating the overall approach.

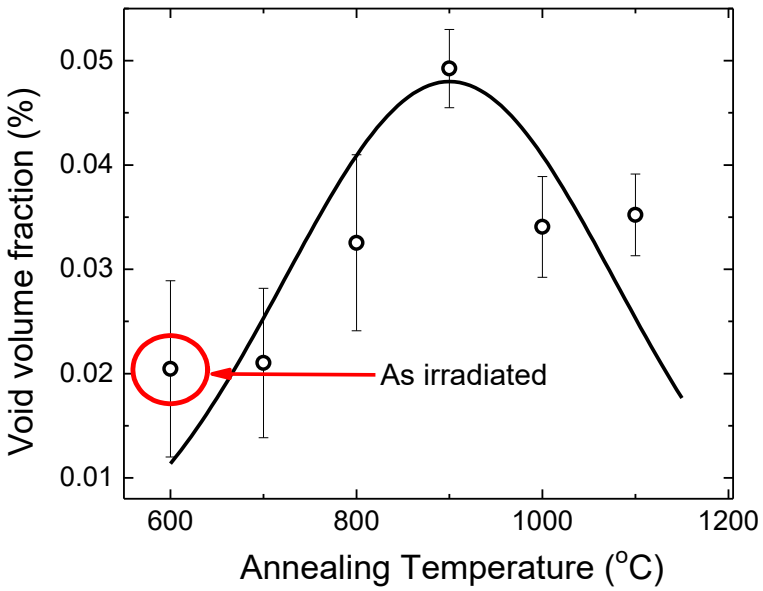

Figure 14. Volume fraction of voids versus annealing temperature. Points (**O**): Experimental data, Line: Simulation (for details see text).

4. Summary and Conclusions

W single crystal was irradiated at the BR2 reactor, at SCK CEN, Mol, Belgium, to 0.11 dpa at 600 °C and it was subsequently isochronally annealed for 24 h up to 1500 °C in steps of 100 °C. As the radiation induced damage results mainly in the formation of vacancy clusters or voids, dislocations loops [8–10] and transmutation products [11–13] the experimental

methods employed, namely (GI)XRD, electrical resistivity, PALS and hardness, were appropriate to quantify the different defects versus annealing temperature and determine their kinetics.

The neutron irradiation of the W(100) single crystal at 600 °C generates dislocation loops having a number density of $(5.4\pm1.1)\times10^{22}$ m^{-3} and an average diameter of (3.0±1.6) nm, whereas the dislocation line density ($(1.6\pm0.4)\times10^{13}$ m^{-2}) is about thirty times smaller (TEM results). Irradiation induced dislocation loops in tungsten appear to have a Burgers vector ½a_0 ⟨111⟩ or a_0 ⟨100⟩, the former being the most commonly observed as they are energetically more favourable [76]. They are of interstitial type with ½a_0 ⟨111⟩ Burgers vector aligned in preferential crystallographic directions as a result of large elastic interactions [77] and form rafts [78]. The dislocation density is reduced versus annealing temperature (Figure 4) and the temperature at which about 5% of the initially neutron produced dislocations remain is $T_{anneal} \sim 1150\,°C$. Such a fast decrease with annealing temperature has been observed in irradiated W with 2 MeV W^+ at 500 °C to a damage of 1.5 dpa [74]. The W^+ irradiation induced loops are of similar diameter to those observed in the as irradiated state of our sample. However, the number density of loops in the self-ion irradiated material is ten times lower than that observed in our neutron irradiated sample. This discrepancy needs to be addressed taking into account that the neutron damage in the current work is around ten times less and the irradiation temperatures are close. The main differences are the damage rates and the sample sizes. The self-ion measurements [74] bring another important aspect of the mechanism of dislocation loops annealing. The reduction of their number is accompanied by the increase of their size versus annealing time and temperature. From this size increase an activation energy of 1.34 to 1.41 eV is calculated. From our data in Figure 4 and a plot (not shown) of $ln\{N_{disl}(T)\}$ versus $1/kT$ for up to 1100 °C an activation energy of (1.6±0.2) eV is obtained. It should be noted that the resistivity measurements (Figure 4) are in concurrence with PALS (Figure 11a, curve of I_a) and hardness measurements (Figure 7). Combining our results and those in the literature, we could make the following remarks regarding the annealing of dislocations: a) there is a fast decrease in their number density versus annealing temperature and above 1100 °C most of them have been annealed, b) the loop size increases with temperature, c) the loop size increases with annealing time indicating a diffusion type process and d) the activation energy for both number density decrease and size increase is around 1.5 eV.

The as irradiated state of single crystal W(100) in addition to dislocations contains voids of density $(8.1\pm3.2)\times10^{22}$ m^{-3} with an average diameter of (1.3±0.2) nm (TEM results). The size of voids increases almost linearly with annealing temperature up to 1100 °C. For example the void size of 1 nm in the as irradiated state increases to 3.5 nm after annealing at 1100 °C. In addition, mono- and di-vacancies produced by irradiation present increased mobility at around 900 °C and coalesce to form small vacancy clusters (Figure 11a, curve I_b). From the simulated curve in Figure 11b it is concluded that the annealing temperature for these vacancy clusters is around 1150 °C. As these clusters dissolve their vacancies are incorporated in the voids and this is confirmed by a “jump” in their size from 3.5 nm at 1100 °C to at least 7 nm at 1200 °C (Figure 10b). The annealing temperature of the large voids is

around 1500 °C and the observed PALS spectrum corresponds to a defect free material. From molecular dynamics calculations it has been found that the dissociation temperature of vacancy clusters increases with vacancy cluster size being around 1100 °C for a size cluster of 60 vacancies [79]. Our results are in agreement with this trend. The observed kinetics of the void dissolution versus annealing temperature is in concurrence with the idea of a critical size [80].

The annealing behaviour of the dislocations and voids discussed above is reflected in the mechanical properties of the material revealed by the hardness measurements. The critical resolved stress arising from dislocations has an annealing temperature $T_{anneal} \sim 1350\,°C$, higher by 200 °C than that obtained from the number density of dislocations determined by resistivity measurements. This arises from the fact that the critical resolved stress due to dislocations is not reduced as fast as the dislocation density, since it depends on the square root of it. The critical resolved stress arising from voids has an annealing temperature $T_{anneal} \sim 1500\,°C$ which is in excellent agreement with the value found from PALS measurements. The 45% increase in hardness induced by neutron irradiation has been completely eliminated after the 1500 °C annealing and the material has reverted to its pre-irradiation state.

The main transmutation product is Re and the calculated concentration by FISPACT-II is 0.38 at%. The other two transmutation products (Os and Ta) are at much lower concentrations (~10^{-3} at%). After 1500 °C annealing, as GIXRD data show, the randomly produced Re isotope has accumulated to larger clusters and also the phases of Re, WRe and WOs_2 are observed.

Finally, it is concluded, that after the annealing at 1500 °C no other defects except Re, WRe and WOs_2 clusters are detectable. Complete defect recovery strongly depends on the irradiation conditions, and it has been observed at various temperatures of 900 °C [31], 1300 °C [36], 1500 °C [32,81] and 1700 °C [75]. Annealing of W components in service in a Fusion reactor would serve to reverse the adverse effects of neutron irradiation. However, this conjecture has to be validated to more heavily damaged W than the one used in the present study and to engineering grade materials.

Acknowledgments

This work has been carried out within the framework of the EUROfusion Consortium and has received funding from the Euratom research and training programme 2014-2018, 2019-2020 and 2021-2025 under Grant Agreements Nos. 633053 and 101052200. The views and opinions expressed herein do not necessarily reflect those of the European Commission. The funding from the Hellenic General Secretariat for Research and Innovation for the Greek National Programme of the Controlled Thermonuclear Fusion is acknowledged. Acknowledgments to the anonymous referee for his/her comments that helped to improve the manuscript.

References

[1] R.A. Pitts, S. Carpentier, F. Escourbiac, T. Hirai, V. Komarov, S. Lisgo, A.S. Kukushkin, A. Loarte, M. Merola, A. Sashala Naik, R. Mitteau, M. Sugihara, B. Bazylev, P.C. Stangeby, A full tungsten divertor for ITER: Physics issues and design status, J. Nucl. Mater. 438 (2013) S48--S56. https://doi.org/10.1016/j.jnucmat.2013.01.008.

[2] G. Pintsuk, Tungsten as a Plasma-Facing Material, in: Compr. Nucl. Mater., Elsevier, Amsterdam, The Netherlands, 2012: pp. 551–581. https://doi.org/10.1016/B978-0-08-056033-5.00118-X.

[3] J.W. Davis, V.R. Barabash, A. Makhankov, L. Plöchl, K.T. Slattery, Assessment of tungsten for use in the ITER plasma facing components, J. Nucl. Mater. 258–263 (1998) 308–312. https://doi.org/10.1016/S0022-3115(98)00285-2.

[4] V. Philipps, Tungsten as material for plasma-facing components in fusion devices, J. Nucl. Mater. 415 (2011) S2--S9. https://doi.org/10.1016/j.jnucmat.2011.01.110.

[5] M. Rieth, R. Doerner, A. Hasegawa, Y. Ueda, M. Wirtz, Behavior of tungsten under irradiation and plasma interaction, J. Nucl. Mater. 519 (2019) 334–368. https://doi.org/10.1016/j.jnucmat.2019.03.035.

[6] A. Hasegawa, M. Fukuda, K. Yabuuchi, S. Nogami, Neutron irradiation effects on the microstructural development of tungsten and tungsten alloys, J. Nucl. Mater. 471 (2016) 175–183. https://doi.org/10.1016/j.jnucmat.2015.10.047.

[7] A. Dubinko, D. Terentyev, C. Yin, W. Van Renterghem, B. Rossaert, M. Rieth, E.E.E. Zhurkin, A. Zinovev, C.C.C. Chang, S. Van Dyck, G. Bonny, Microstructure and hardening induced by neutron irradiation in single crystal, ITER specification and cold rolled tungsten, Int. J. Refract. Met. Hard Mater. 98 (2021) 105522. https://doi.org/10.1016/j.ijrmhm.2021.105522.

[8] J.A. Brinkman, On the Nature of Radiation Damage in Metals, J. Appl. Phys. 25 (1954) 961–970. https://doi.org/10.1063/1.1721810.

[9] J.T. Buswell, Vacancy damage in heavy ion and neutron-irradiated tungsten, Philos. Mag. 22 (1970) 787–802. https://doi.org/10.1080/14786437008220947.

[10] R.C. Rau, R.L. Ladd, J. Moteff, Voids in irradiated tungsten and molybdenum, J. Nucl. Mater. 33 (1969) 324–327. https://doi.org/10.1016/0022-3115(69)90029-4.

[11] M. Klimenkov, U. Jäntsch, M. Rieth, H.C.C. Schneider, D.E.J.E.J. Armstrong, J. Gibson, S.G.G. Roberts, Effect of neutron irradiation on the microstructure of tungsten, Nucl. Mater. Energy. 9 (2016) 480–483. https://doi.org/10.1016/j.nme.2016.09.010.

[12] M.J. Lloyd, R.G. Abernethy, M.R. Gilbert, I. Griffiths, P.A.J.J. Bagot, D. Nguyen-Manh, M.P. Moody, D.E.J.J. Armstrong, Decoration of voids with rhenium and osmium transmutation products in neutron irradiated single crystal tungsten, Scr. Mater. 173 (2019) 96–100. https://doi.org/10.1016/j.scriptamat.2019.07.036.

[13] M.R.R. Gilbert, J.-C. Sublet, Neutron-induced transmutation effects in W and W-alloys in a fusion environment, Nucl. Fusion. 51 (2011) 43005. https://doi.org/10.1088/0029-5515/51/4/043005.

[14] A. Hasegawa, M. Fukuda, S. Nogami, K. Yabuuchi, Neutron irradiation effects on tungsten materials, Fusion Eng. Des. 89 (2014) 1568–1572.

https://doi.org/10.1016/j.fusengdes.2014.04.035.

[15] Y. Katoh, L.L. Snead, L.M. Garrison, X. Hu, T. Koyanagi, C.M. Parish, P.D. Edmondson, M. Fukuda, T. Hwang, T. Tanaka, A. Hasegawa, Response of unalloyed tungsten to mixed spectrum neutrons, J. Nucl. Mater. 520 (2019) 193–207. https://doi.org/10.1016/j.jnucmat.2019.03.045.

[16] A. Mannheim, J.A.W. van Dommelen, M.G.D. Geers, Controlled irradiation hardening of tungsten by cyclic recrystallization, Model. Simul. Mater. Sci. Eng. 27 (2019) 65001. https://doi.org/10.1088/1361-651X/ab1eec.

[17] H.-C. Schneider, C. Petersen, A.V. V Povstyanko, A.E.E. Fedoseev, O. Makarov, Repeatability of irradiation damage and of recovery by post-irradiation annealing of EUROFER base steels, Fusion Eng. Des. 124 (2017) 1019–1023. https://doi.org/10.1016/j.fusengdes.2017.04.066.

[18] M.W. Thompson, The damage and recovery of neutron irradiated tungsten, Philos. Mag. 5 (1960) 278–296. https://doi.org/10.1080/14786436008235842.

[19] L.K. Keys, J.P. Smith, J. Moteff, High-temperature recovery of tungsten after neutron irradiation, Phys. Rev. 176 (1968) 851–856. https://doi.org/10.1103/PhysRev.176.851.

[20] L.K. Keys, J. Moteff, Comparison of the Recovery of Damage in W and Mo after Neutron Irradiation, J. Appl. Phys. 40 (1969) 3866–3868. https://doi.org/10.1063/1.1658291.

[21] L.K. Keys, J. Moteff, Neutron irradiation and defect recovery of tungsten, J. Nucl. Mater. 34 (1970) 260–280. https://doi.org/10.1016/0022-3115(70)90193-5.

[22] V.N. Bykov, G.A. Birzhevoi, M.I. Zakharova, V.A. Solov'ev, Nature and thermal stability of radiation defects in single-crystal tungsten, Sov. At. Energy. 33 (1972) 930–935. https://doi.org/10.1007/BF01666749.

[23] M.I. Zakharova, V.A. Solov'ev, V.N. Bykov, High-temperature stages of the annealing of radiation defects in refractory BCC metals, Sov. At. Energy. 38 (1975) 101–104. https://doi.org/10.1007/BF01208865.

[24] Y.-W.W. Kim, J.M.M. Galligan, Radiation damage and stage iii defect annealing in thermal neutron irradiated tungsten, Acta Metall. 26 (1978) 379–390. https://doi.org/10.1016/0001-6160(78)90165-7.

[25] K. Young-Won, J.M. Galligan, An annealing study of thermal neutron irradiated tungsten, J. Nucl. Mater. 69–70 (1978) 680–682. https://doi.org/10.1016/0022-3115(78)90312-4.

[26] M.S. Anand., B.M. Pande, R.P. Agarwala, Recovery in neutron irradiated tungsten, Radiat. Eff. 39 (1978) 149–155. https://doi.org/10.1080/00337577808234468.

[27] D. Jeannotte, J.M. Galligan, Energy of motion of vacancies in tungsten, Phys. Rev. Lett. 19 (1967) 232–233. https://doi.org/10.1103/PhysRevLett.19.232.

[28] D. Jeannotte, J.M. Galligan, A study of radiation damage in tungsten-I, Acta Metall. 18 (1970) 71–79. https://doi.org/10.1016/0001-6160(70)90070-2.

[29] O. V. Ogorodnikova, Y. Gasparyan, V. Efimov, Ciupiński, J. Grzonka, V.O. Ogorodnikova, Y. Gasparyan, V. Efimov, Ciupiński, J. Grzonka, Annealing of radiation-induced damage in tungsten under and after irradiation with 20 MeV self-ions, J. Nucl. Mater. 451 (2014) 379–386. https://doi.org/10.1016/j.jnucmat.2014.04.011.

[30] J. Grzonka, Ciupiński, J. Smalc-Koziorowska, O. V. Ogorodnikova, M. Mayer, K.J. Kurzydłowski, V.O. Ogorodnikova, M. Mayer, K.J. Kurzydłowski, Electron microscopy observations of radiation damage in irradiated and annealed tungsten, Nucl. Instruments Methods Phys. Res. Sect. B Beam Interact. with Mater. Atoms. 340 (2014) 27–33. https://doi.org/10.1016/j.nimb.2014.07.043.

[31] V.O. Ogorodnikova, L.Y. Dubov, V.S. Stepanov, D. Terentyev, V.Y. Funtikov, V.Y. Shtotsky, V.S. Stolbunov, V. Efimov, K. Gutorov, O. V. Ogorodnikova, L.Y. Dubov, S. V. Stepanov, D. Terentyev, Y. V. Funtikov, Y. V. Shtotsky, V.S. Stolbunov, V. Efimov, K. Gutorov, Annealing of radiation-induced defects in tungsten: Positron annihilation spectroscopy study, J. Nucl. Mater. 517 (2019) 148–151. https://doi.org/10.1016/j.jnucmat.2019.02.010.

[32] M. Zibrov, W. Egger, J. Heikinheimo, M. Mayer, F. Tuomisto, Vacancy cluster growth and thermal recovery in hydrogen-irradiated tungsten, J. Nucl. Mater. 531 (2020) 152017. https://doi.org/10.1016/j.jnucmat.2020.152017.

[33] B. Horvath, Y. Dai, Y. Lee, Annealing effect on the microstructure of tungsten irradiated in SINQ target, J. Nucl. Mater. 506 (2018) 19–25. https://doi.org/10.1016/J.JNUCMAT.2017.12.020.

[34] P.E. Lhuillier, M.F. Barthe, P. Desgardin, W. Egger, P. Sperr, Positron annihilation studies on the nature and thermal behaviour of irradiation induced defects in tungsten, Phys. Status Solidi. 6 (2009) 2329–2332. https://doi.org/10.1002/pssc.200982114.

[35] P.M.G.G. Nambissan, P. Sen, Positron annihilation study of the annealing behaviour of alpha induced defects in tungsten, Radiat. Eff. Defects Solids. 124 (1992) 215–221. https://doi.org/10.1080/10420159208220193.

[36] X. Hu, T. Koyanagi, M. Fukuda, Y. Katoh, L.L. Snead, B.D. Wirth, Defect evolution in single crystalline tungsten following low temperature and low dose neutron irradiation, J. Nucl. Mater. 470 (2016) 278–289. https://doi.org/10.1016/j.jnucmat.2015.12.040.

[37] M.J. Norgett, M.T. Robinson, I.M. Torrens, A proposed method of calculating displacement dose rates, Nucl. Eng. Des. 33 (1975) 50–54. https://doi.org/10.1016/0029-5493(75)90035-7.

[38] V. Chatzikos, K. Mergia, G. Bonny, D. Terentyev, D. Papadakis, G.E. Pavlou, S. Messoloras, International Journal of Refractory Metals and Hard Materials Positron annihilation spectroscopy investigation of defects in neutron irradiated tungsten materials Cross section along, Int. J. Refract. Met. Hard Mater. 105 (2022) 105838. https://doi.org/10.1016/j.ijrmhm.2022.105838.

[39] K. Mergia, V. Chatzikos, E. Manios, S. Dellis, D. Papadakis, D. Terentyev, G. Bonny, A. Dubinko, I.E. Stamatelatos, S. Messoloras, M. Rieth, Evolution of microstructure in neutron irradiated cold rolled tungsten and its correlation with hardness, Fusion Eng. Des. 172 (2021) 112784. https://doi.org/10.1016/j.fusengdes.2021.112784.

[40] D. Giebel, J. Kansy, A New Version of LT Program for Positron Lifetime Spectra Analysis, Mater. Sci. Forum. 666 (2010) 138–141. https://doi.org/10.4028/www.scientific.net/MSF.666.138.

[41] D. Giebel, J. Kansy, LT10 Program for Solving Basic Problems Connected with Defect Detection, Phys. Procedia. 35 (2012) 122–127. https://doi.org/10.1016/j.phpro.2012.06.022.

[42] X. Yi, A.E. Sand, D.R. Mason, M.A. Kirk, S.G. Roberts, K. Nordlund, S.L. Dudarev,

Direct observation of size scaling and elastic interaction between nano-scale defects in collision cascades, EPL (Europhysics Lett. 110 (2015) 36001. https://doi.org/10.1209/0295-5075/110/36001.

[43] C. Berne, M. Sluiter, Y. Kawazoe, A. Pasturel, Ordering effects in the Re–W and Re–Ta sigma phases, J. Phys. Condens. Matter. 13 (2001) 9433–9443. https://doi.org/10.1088/0953-8984/13/42/304.

[44] M. Dürrschnabel, M. Klimenkov, U. Jäntsch, M. Rieth, H.C. Schneider, D. Terentyev, New insights into microstructure of neutron-irradiated tungsten, Sci. Rep. 11 (2021) 1–17. https://doi.org/10.1038/s41598-021-86746-6.

[45] M. Fukuda, N.A.P.P. Kiran Kumar, T. Koyanagi, L.M. Garrison, L.L. Snead, Y. Katoh, A. Hasegawa, Neutron energy spectrum influence on irradiation hardening and microstructural development of tungsten, J. Nucl. Mater. 479 (2016) 249–254. https://doi.org/10.1016/j.jnucmat.2016.06.051.

[46] P.D. Edmondson, B. Gault, M.R. Gilbert, An atom probe tomography and inventory calculation examination of second phase precipitates in neutron irradiated single crystal tungsten, Nucl. Fusion. 60 (2020). https://doi.org/10.1088/1741-4326/abb149.

[47] D. Nguyen-Manh, J.S. Wróbel, M. Klimenkov, M.J. Lloyd, L. Messina, S.L. Dudarev, First-principles model for voids decorated by transmutation solutes: Short-range order effects and application to neutron irradiated tungsten, Phys. Rev. Mater. 5 (2021) 1–23. https://doi.org/10.1103/PhysRevMaterials.5.065401.

[48] P.L. Rossiter, The electrical resistivity of metals and alloys, Electr. Resist. Met. Alloy. (1987). https://doi.org/10.1017/cbo9780511600289.

[49] J.W. Martin, R. Paetsch, Electrical resistivity of voids, J. Phys. F Met. Phys. 3 (1973) 907–917. https://doi.org/10.1088/0305-4608/3/5/005.

[50] J.W. Martin, The electrical resistivity due to structural defects, Philos. Mag. 24 (1971) 555–566. https://doi.org/10.1080/14786437108217029.

[51] J.W. Martin, The electrical resistivity of some lattice defects in FCC metals observed in radiation damage experiments, J. Phys. F Met. Phys. 2 (1972) 842–853. https://doi.org/10.1088/0305-4608/2/5/008.

[52] K.-D.D. Rasch, R.W. Siegel, H. Schultz, Quenching and recovery investigations of vacancies in tungsten, Philos. Mag. A. 41 (1980) 91–117. https://doi.org/10.1080/01418618008241833.

[53] L. Uray, P. Tekula-Buxbaum, Resistivity contribution of solutes in tungsten, J. Less Common Met. 123 (1986) 95–100. https://doi.org/10.1016/0022-5088(86)90119-0.

[54] T. Tanno, A. Hasegawa, M. Fujiwara, J.C. He, S. Nogami, M. Satou, T. Shishido, K. Abe, Precipitation of solid transmutation elements in irradiated tungsten alloys, Mater. Trans. 49 (2008) 2259–2264. https://doi.org/10.2320/matertrans.MAW200821.

[55] P. Filippov, U. Koch, Nanoindentation of Aluminum Single Crystals: Experimental Study on Influencing Factors, Materials (Basel). 12 (2019) 3688. https://doi.org/10.3390/ma12223688.

[56] S. Dellis, X. Xiao, D. Terentyev, K. Mergia, S. Krimpalis, A. Bakaev, S. Messoloras, Mechanical properties of neutron-irradiated single crystal tungsten W(100) studied by indentation and FEM modelling, J. Nucl. Mater. 551 (2021) 152985. https://doi.org/10.1016/j.jnucmat.2021.152985.

[57] D.E. Laughlin, K. Hono, Physical Metallurgy: Fifth Edition, Elsevier, 2014. https://doi.org/10.1016/C2010-0-65716-6.

[58] C. Yin, G. Bonny, D. Terentyev, Anisotropy in the hardness of single crystal tungsten before and after neutron irradiation, J. Nucl. Mater. 546 (2021) 152759. https://doi.org/10.1016/j.jnucmat.2020.152759.

[59] R. Royce, M.S. Section, B.R. Board, Anisotropy in the hardness of single crystals, Proc. R. Soc. London. A. Math. Phys. Sci. 322 (1971) 73–88. https://doi.org/10.1098/rspa.1971.0055.

[60] D. Tabor, The physical meaning of indentation and scratch hardness, Br. J. Appl. Phys. 7 (1956) 159–166. https://doi.org/10.1088/0508-3443/7/5/301.

[61] X. Hu, T. Koyanagi, M. Fukuda, N.A.P.K. Kumar, L.L. Snead, B.D. Wirth, Y. Katoh, Irradiation hardening of pure tungsten exposed to neutron irradiation, J. Nucl. Mater. 480 (2016) 235–243. https://doi.org/10.1016/j.jnucmat.2016.08.024.

[62] R.E.E. Stoller, S.J.J. Zinkle, On the relationship between uniaxial yield strength and resolved shear stress in polycrystalline materials, J. Nucl. Mater. 283–287 (2000) 349–352. https://doi.org/10.1016/S0022-3115(00)00378-0.

[63] S.. J. Zinkle, Y. Matsukawa, Observation and analysis of defect cluster production and interactions with dislocations, J. Nucl. Mater. 329–333 (2004) 88–96. https://doi.org/10.1016/j.jnucmat.2004.04.298.

[64] D. Terentyev, X. Xiao, A. Dubinko, A. Bakaeva, H. Duan, Dislocation-mediated strain hardening in tungsten: Thermo-mechanical plasticity theory and experimental validation, J. Mech. Phys. Solids. 85 (2015) 1–15. https://doi.org/10.1016/j.jmps.2015.08.015.

[65] V.S.S. Subrahmanyam, P.M.G.M.G. Nambissan, P. Sen, Helium bubbles in tungsten studied by positron annihilation, Solid State Commun. 89 (1994) 523–527. https://doi.org/10.1016/0038-1098(94)90749-8.

[66] C.L. Dube, P.K. Kulriya, D. Dutta, P.K. Pujari, Y. Patil, M. Mehta, P. Patel, S.S. Khirwadkar, Positron annihilation lifetime measurement and X-ray analysis on 120 MeV Au+7 irradiated polycrystalline tungsten, J. Nucl. Mater. 467 (2015) 406–412. https://doi.org/10.1016/j.jnucmat.2015.05.029.

[67] T. Troev, E. Popov, N. Nankov, T. Yoshiie, Model calculation of positron states in tungsten containing hydrogen and helium, J. Phys. Conf. Ser. 207 (2010) 12033. https://doi.org/10.1088/1742-6596/207/1/012033.

[68] S. Zhu, Y. Xu, Z. Wang, Y. Zheng, D. Zhou, E. Du, D. Yuan, M. Fukuda, M. Mihara, K. Matsuta, T. Minamisono, Positron annihilation lifetime spectroscopy on heavy ion irradiated stainless steels and tungsten, J. Nucl. Mater. 343 (2005) 330–332. https://doi.org/10.1016/j.jnucmat.2004.11.024.

[69] J. De Vries, Positron Lifetime Technique with Applications in Material Science, 1987.

[70] J. Heikinheimo, K. Mizohata, J. Räisänen, T. Ahlgren, P. Jalkanen, A. Lahtinen, N. Catarino, E. Alves, F. Tuomisto, Direct observation of mono-vacancy and self-interstitial recovery in tungsten, APL Mater. 7 (2019) 21103. https://doi.org/10.1063/1.5082150.

[71] A. Yabuuchi, M. Tanaka, A. Kinomura, Short positron lifetime at vacancies observed in electron-irradiated tungsten: Experiments and first-principles calculations, J. Nucl. Mater. 542 (2020) 152473. https://doi.org/10.1016/j.jnucmat.2020.152473.

[72] A. Balogh, I. Dézsi, Further Positron Lifetimes of Some Elements, Phys. Status Solidi. 81 (1977) K81--K82. https://doi.org/10.1002/pssb.2220810241.

[73] M. Eldrup, B.N.N. Singh, Studies of defects and defect agglomerates by positron annihilation spectroscopy, J. Nucl. Mater. 251 (1997) 132–138. https://doi.org/10.1016/S0022-3115(97)00221-3.

[74] F. Ferroni, X. Yi, K. Arakawa, S.P. Fitzgerald, P.D. Edmondson, S.G. Roberts, High temperature annealing of ion irradiated tungsten, Acta Mater. 90 (2015) 380–393. https://doi.org/10.1016/j.actamat.2015.01.067.

[75] M. Zibrov, T. Dürbeck, W. Egger, M. Mayer, High temperature recovery of radiation defects in tungsten and its effect on deuterium retention, Nucl. Mater. Energy. 23 (2020) 100747. https://doi.org/10.1016/j.nme.2020.100747.

[76] J. Fikar, R. Schäublin, Atomistic simulations of nanometric dislocation loops in bcc tungsten, Nucl. Instruments Methods Phys. Res. Sect. B Beam Interact. with Mater. Atoms. 267 (2009) 3218–3222. https://doi.org/10.1016/j.nimb.2009.06.075.

[77] S.L. Dudarev, M.R. Gilbert, K. Arakawa, H. Mori, Z. Yao, M.L. Jenkins, P.M. Derlet, Langevin model for real-time Brownian dynamics of interacting nanodefects in irradiated metals, Phys. Rev. B. 81 (2010) 224107. https://doi.org/10.1103/PhysRevB.81.224107.

[78] S. Hasanzadeh, R. Schäublin, B. Décamps, V. Rousson, E. Autissier, M.F. Barthe, C. Hébert, Three-dimensional scanning transmission electron microscopy of dislocation loops in tungsten, Micron. 113 (2018) 24–33. https://doi.org/10.1016/j.micron.2018.05.010.

[79] J. Fikar, R. Schäublin, Stability of small vacancy clusters in tungsten by molecular dynamics, Nucl. Instruments Methods Phys. Res. Sect. B Beam Interact. with Mater. Atoms. 464 (2020) 56–59. https://doi.org/10.1016/j.nimb.2019.11.044.

[80] I. Rovelli, S.L. Dudarev, A.P. Sutton, Non-local model for diffusion-mediated dislocation climb and cavity growth, J. Mech. Phys. Solids. 103 (2017) 121–141. https://doi.org/10.1016/j.jmps.2017.03.008.

[81] M.I. Zakharova, N.A. Artemov, V. V. Bogdanov, Effects of neutron irradiation and annealing on the elastic moduli and electrical resistivity of molybdenum and tungsten single crystals, Inorg. Mater. 37 (2001) 786–789. https://doi.org/10.1023/A:1017979230262.